Materials Advances

ROYAL SOCIETY OF CHEMISTRY

PAPER

View Article Online
View Journal | View Issue

Cite this: *Mater. Adv.*, 2025, 6, 263

Finding low-toxicity biopolymer solvents with high melting temperature and thermally induced phase separation of poly(ε-caprolactone)†

Patrik Boura,[ab] Lenka Krajakova,[a] Adam Bouz,[a] Silvestr Figalla,[c] Alexandr Zubov,[a] Bart Van der Bruggen[b] and Juraj Kosek*[a]

Received 14th October 2024,
Accepted 27th November 2024

DOI: 10.1039/d4ma01033g

rsc.li/materials-advances

This study focuses on identifying low-toxicity solvents for biopolymers such as poly(ε-caprolactone) (PCL) and polylactic acid (PLA) for applications in thermally induced phase separation (TIPS). Common solvents like dioxane and tetrahydrofuran, despite their effectivity, pose significant health risks. Therefore, this research aims to expand the available knowledge of safer solvent alternatives with melting temperatures above 0 °C to enhance the economic and environmental viability of TIPS. The Hansen solubility theory was applied to screen 846 chemicals for their compatibility with biopolymers, selecting those with favourable properties and experimentally testing their potential as TIPS solvents. Among the newly identified solvents, methyl-*p*-toluate (MPTOL) exhibited superior performance for PCL, showing high dissolution efficiency, low toxicity, and a melting temperature of 34 °C. The phase diagram of the PCL/MPTOL system was constructed using experimental data and computational modelling based on Flory–Huggins theory and PC-SAFT equation of state. Foams prepared through TIPS from this system demonstrated three distinct morphologies with increasing PCL concentration, aligning with expectations based on the phase diagram. These findings present methyl-*p*-toluate as a promising, safer alternative solvent for biopolymer processing in tissue engineering and membrane technologies, with potential to reduce energy costs and enhance process efficiency.

1. Introduction

Nano and micro-cellular polymeric materials have diverse application possibilities and can be made by a plethora of preparative methods. Certain high added value materials such as membranes or tissue engineering scaffolds require tailored properties corresponding to their purpose. Common denominators are high porosity,[1–3] permeability,[4–6] good mechanical properties,[2–4,7,8] and specific pore sizes.[1,4,5,9] Moreover, scaffold applications further require biocompatibility[3,9–12] and biodegradability.[13,14]

These requirements can be potentially fulfilled by thermally induced phase separation (TIPS) utilizing a phase inversion process in a quenched polymer solution. It is a simple method, achieving high porosity and low defects content,[15] which can be easily combined with other fabrication methods.[16] In summary, TIPS consists of three steps: (1) dissolving a polymer in a solvent at temperature above the critical solution temperature (T_c), (2) quenching the resulting polymer solution below binodal curve (*cf.* Fig. 1) to induce phase separation, (3) removing the solvent by lyophilization, extraction or evaporation.[17,18] Phase separation should take place mostly below the spinodal curve (*cf.* Fig. 1), in the unstable region, to facilitate spinodal decomposition and to obtain the open-pore structure desired in membrane and scaffold applications. The solution de-mixing into interconnected polymer-rich and polymer-lean phases during spinodal decomposition, can be stopped by reaching a temperature below the freezing temperature (T_f) of both phases.[19] This can be advantageous to obtain a sufficiently low pore size, which is influenced by the quenching speed, *i.e.*, the final cooling temperature.[20]

However, cooling the polymer system below its T_f (*cf.* Fig. 1) necessitates the use of solvents with high melting temperature, ideally above 0 °C, to ensure the economic viability of the method, as cooling is an energetically intensive process required during the initial temperature quench as well as subsequent solvent removal. This considerably reduces the number of known viable biopolymer solvents and the few known are often carcinogenic, making their use problematic, at the very least, in tissue engineering applications.

Common, FDA approved, biopolymers used for TIPS scaffold preparation are polylactic acid (PLA) and poly(ε-caprolactone)

[a] *Department of Chemical Engineering, University of Chemistry and Technology Prague, Technická 5, 166 28 Prague 6, Czech Republic. E-mail: Juraj.Kosek@vscht.cz*
[b] *Department of Chemical Engineering, KU Leuven, Celestijnenlaan 200F, B-3001 Leuven, Belgium*
[c] *Institute of Materials Chemistry, Faculty of Chemistry, Brno University of Technology, Brno 61200, Czech Republic*

† Electronic supplementary information (ESI) available. See DOI: https://doi.org/10.1039/d4ma01033g

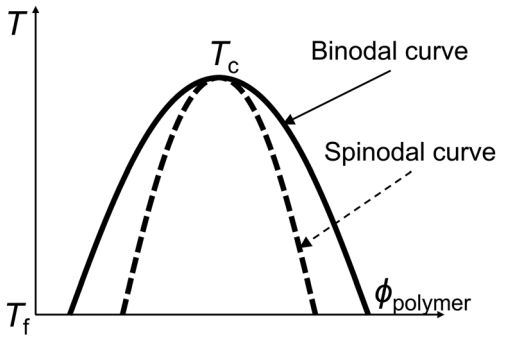

Fig. 1 Simplified visualization of typical binary upper critical solution temperature (UCST) polymer/solvent phase diagram, including critical temperature T_c at the intersection of binodal and spinodal curve, volume fraction of polymer ($\phi_{polymer}$) on horizontal axis and temperature (T) on vertical axis. In practice, phase diagram shape can be influenced by number of factors such as polydispersity, while T_f can be dependent on solution composition.

(PCL), which are advantageous for TE applications due to the low toxicity of their degradation products and their ability to fully metabolize in the body.[15]

In the literature, PLA[21–23] and PCL[24–26] are often dissolved in 1,4-dioxane, which is a known carcinogen[27] with T_m = 11.8 °C.[28] Tetrahydrofuran (THF), suspected of causing cancer,[29] T_m = −108.4 °C,[30] was used as PLA[31] as well as PCL[25] TIPS solvent. Dimethyl sulfoxide (DMSO), T_m = 17.9 °C,[32] classified by FDA in the same group as ethanol,[33] was used to dissolve PCL,[26] although recent research by Verheijen *et al.* suggests caution while using DMSO, recommending its avoidance where possible.[33] Example of a PCL TIPS solvent, approved by FDA, is ethyl lactate;[34] however, its notable disadvantage lies in its relatively low T_m = −26 °C.[35]

In this work, the focus is on broadening the current application areas of TIPS by finding viable novel low-toxicity PCL and PLA solvents. Firstly, the Hansen solubility theory was utilized to theoretically compare 846 chemicals and their dissolution potential of respective biopolymers. Secondly, chemicals with $T_m > 0$ °C, reasonably low toxicity and purchase cost were chosen, and subsequently experimentally tested. Thirdly, the newly found system of PCL dissolved in methyl-*p*-toluate (MPTOL) was further studied, investigating its phase diagram, using experimental measurements complemented by computational models, and preparing porous materials using TIPS, while investigating the influence of the composition of the solution on the final morphology, both qualitatively and quantitatively.

2. Methodology

2.1 Solvent screening *via* Hansen solubility parameters

The Hansen solubility theory was used for finding novel low toxicity solvents suitable for TIPS. An in-house Excel TIPS solvent finding tool was created by combination of Hansen solubility parameters (HSP), taken from a handbook,[36] together with boiling temperatures T_b and melting temperatures T_m of respective potential solvents. This allowed, after chemical name corrections and removal of duplicates, quick scanning of 846 chemicals and their solubility potential with respect to the studied biopolymers.

Table 1 Biopolymer HSP parameters taken from literature: (a) PCL measured by swelling tests, (b) PLA taken from HSP website,[38] (c) determined using inverse gas chromatography (IGC),[39] and taken from book sources (d) ref. 40 and (e) ref. 41

Polymer	Ref.	δ_D ($MPa^{1/2}$)	δ_P ($MPa^{1/2}$)	δ_H ($MPa^{1/2}$)
PCL	42	17.8	6.2	7.7
PLA	38	18.72	7	7
	39	19.8	4	6.7
	40	18.88	4.61	7.61
	41	18.6	9.9	6

PCL and PLA HSP parameters were taken from the literature (*cf.* Table 1). The PCL HSP were found for a polymer with similar chain length to ours and thus only one set of parameters was used. On the contrary, PLA HSP literature sources lacked polymer description, and therefore four different sets of parameters were evaluated to broaden the range of viable solvents tested. Each of the HSP represents a different type of interactions, where: (1) δ_D represents non-polar interactions, also called dispersion interactions, derived from atomic forces, (2) δ_P represents permanent dipole–permanent dipole interactions, and (3) δ_H represents hydrogen bonding.[37]

To account for elevated temperature during experimental conditions, the temperature dependency of the HSP (δ_D, δ_P, δ_H) was utilized:[37]

$$\delta_{Dh} = \delta_D \cdot (1 - \Delta T \cdot 1.25\alpha), \quad (1)$$

$$\delta_{Ph} = \delta_P \cdot (1 - \Delta T \cdot 0.5\alpha), \quad (2)$$

$$\delta_{Hh} = \delta_H \cdot (1 - \Delta T \cdot (1.22 \times 10^{-3} + 0.5\alpha)), \quad (3)$$

where subscript suffix h stands for heated, ΔT is a temperature difference between heated state and original HSP temperature, usually 25 °C, and α stands for thermal expansion coefficient chosen to be a constant equal to 7×10^{-4} K^{-1} for all solvent candidates. The distance R_a between biopolymer/solvent pairs in the Hansen solubility space was calculated as:

$$(R_a)^2 = 4(\delta_{Dh2} - \delta_{Dh1})^2 + (\delta_{Ph2} - \delta_{Ph1})^2 + (\delta_{Hh1} - \delta_{Hh2})^2, \quad (4)$$

and the presence inside/outside of Hansen solubility sphere with a size quantified by parameter R_0, *cf.* Fig. 2, was evaluated based on the relative energy difference (RED) as follows:

$$RED = R_a/R_0 \leq 1 \ldots \text{solvent candidate},$$

$$RED = R_a/R_0 > 1 \ldots \text{non-solvent}.$$

Toxicity score was given to solvents to divide them into three groups: low-toxicity (1), mid-toxicity (2), and high-toxicity (3). Solvents were placed in the high-toxicity group, if they have been at least suspected of causing cancer, teratogenicity, damage to fertility and children or otherwise causing serious

Table 2 List of tested chemicals and their Hazard statements[29]

Chemical	CAS number	Hazard statements
o-Bromoanisole	578-57-4	H315, H319, H412
trans-Anethole	4180-23-8	H317, H411
p-Bromotoluene	106-38-7	H332, H411
Benzoic acid	65-85-0	H315, H318, H372
Methyl *p*-toluate	99-75-2	H315, H319, H335
Ethyl cinnamate	103-36-6	—
Dibenzyl ether	103-50-4	H317, H410
Dimethyl phthalate	131-11-3	—
2,4-Dichlorobenzaldehyde	874-42-0	H314, H318, H411
4′-Methoxyacetophenone	100-06-1	H302
1-Decanol	112-30-1	H319, H412
p-Chlorobenzoyl chloride	122-01-0	H314, H318, H412
4-Bromophenetole	588-96-5	H315, H319, H335
4-Chloro-2-nitrotoluene	89-59-8	H315, H319, H335
Acetophenone	98-86-2	H302, H319

damage to humans due to inhalation. In terms of GHS hazard statements, the high-toxicity group included solvents with at least some of the following health hazards: H330-331, H340-341, H350-351, H360-362, H370-372. On the contrary, the low-toxicity group was defined for solvents causing at worst respiratory irritation or other hazards common for pure chemicals in contact with respective body part such as eye or skin irritation. Therefore, the following health hazards statements were allowed for solvent placement in the low-toxicity group: H302-303, H313-320. The rest of the solvents was placed in the mid-toxicity group.

Additionally, relative solvent purchase costs at Sigma Aldrich (Merck) were indicated in three levels based on price per 100 g, as follows: (i) low-cost ($): below 100 USD, (ii) mid-cost ($$): 100 – 200 USD, (iii) high-cost ($$): 200 USD and above. Solvent selection procedure is further discussed in Section 3.1.

2.2 Materials

Polylactic acid (PLA) pellets (~3 mm), with defined melt flow rate MFR = 6 g/10 min, density ρ_{PLA} = 1050 kg m^{-3} (at 25 °C), and PLA pellets (3–5 mm), with defined MFR = 80 g/10 min were purchased from Goodfellow Cambridge Limited, United Kingdom. The two PLA variations are further referred to as PLA6 and PLA80 based on their respective MFR. Polycaprolactone (PCL) pellets (~3 mm), M_n = 80 kDa as indicated by manufacturer, ρ_{PCL} = 1145 kg m^{-3} (at 25 °C) were obtained from Sigma Aldrich (Merck). All of the used biopolymers were further characterized by gel permeation chromatography (GPC) with results presented in Section 3.1 and with implications discussed further in Section 3.2. Solvents 1-decanol (98% purity), 2,4-dichlorobenzaldehyde (99% purity), *o*-bromoanisole (97% purity), *p*-bromotoluene (98% purity), 4-methoxyacetophenone (99% purity), dibenzyl ether (98% purity), dimethyl phthalate (99% purity), ethyl cinnamate (98% purity), benzoic acid (99.5% purity), *trans*-anethole (99% purity), *p*-chlorobenzoyl chloride (99% purity), 4-bromophenetole (98% purity), acetophenone (99% purity), 4-chloro-2-nitrotoluene (99.8% purity) were purchased from Sigma Aldrich (Merck). Methyl *p*-toluate (MPTOL, 99% purity), purchased from Sigma Aldrich (Merck), was used as a PCL solvent during TIPS foaming experiments, whilst ethanol (96% purity) purchased from Lach-Ner, s.r.o., Neratovice (CZ) was used as an extraction agent. The initial PCL fraction in the foaming solution was 8, 10, 12, 14, and 16 wt% (7.4, 9.3, 11.2, 13.1, and 15.0 vol%, respectively) These concentrations were chosen for three reasons: (i) the PCL concentration had to be high enough to prepare mechanically stable foams, (ii) it had to be low enough to ensure low viscosity, *i.e.*, sufficiently quick transfer from glass tube to foaming cell, (iii) and to achieve prevalent phase separation by spinodal decomposition leading to formation of interconnected structure. The initial solution was preheated to the initial temperature T_{init} = 70 °C, poured into the vessel preheated to 50 °C and then quenched in a cooling bath with dry ice kept at cooling temperature T_{cool} = −78.5 °C.

2.3 Cloud point and freezing point measurement apparatus

Two in-house built measurement apparatus variations, schematically presented in Fig. 3, were used to experimentally determine binary polymer–solvent phase diagram.

The first variation, used to measure cloud points (*i.e.*, binodal points), utilized optometric measurement (*i.e.*, turbidimetry; *cf.* Fig. 3(a)). The cloud point apparatus included: (aA) enclosed removable test tube with magnetically stirred polymer–solvent solution and immersed PT-100 sensor, (aB) glass cooling bath connected to (aC) programmable thermostat with a cooling option, (aE) 10 mW laser source emitting a laser beam passing through the polymer solution to the (aF) PDA 100A-EC Si amplified photodetector connected, together with the PT-100 sensor, to the data collection system (aD). The relevant parts of the setup were placed in a black box to minimize the interference caused by other light sources. The data collection system consisted of data acquisition card (DAQ) converting the analogue sensor input to digital output, connected by USB to PC, further processed by a LabView software recording temperature, and the photodetector signal. This setup allows precise temperature control of ±0.01 °C and cloud point temperature determination based on decrease in photodetector signal after phase separation at the measured temperature.

The second variation (Fig. 3(b)), utilized for freezing point measurements, was based on measurements of temperature evolution in time. The polymer–solvent solution was gradually cooled down in the inner part of double-layer glass cell with a cooling agent flowing through its walls (bB). At the freezing temperature T_f, the tested solution starts to release heat equal to its enthalpy of freezing changing the temperature-evolution profile and allowing the determination of freezing temperature following linear data interpolation and comparison of temperature profiles before and after solidification. The cooling cell (bB) allows measurement with ≈15 ml of polymer–solvent solutions, compared to ≈3 ml used in setup (a), leading to a more pronounced change in the measured temperature evolution profile. Additionally, thermal insulation was applied to both the cell and the silicon tubing allowing measurement between −20 to 150 °C. The rest of the second apparatus (Fig. 3(b)) is analogous to the first one (Fig. 3(a)).

2.4 Mathematical modelling of phase diagram curves

The polymer/solvent phase diagram has been calculated using two thermodynamical models: (1) the Flory–Huggins lattice

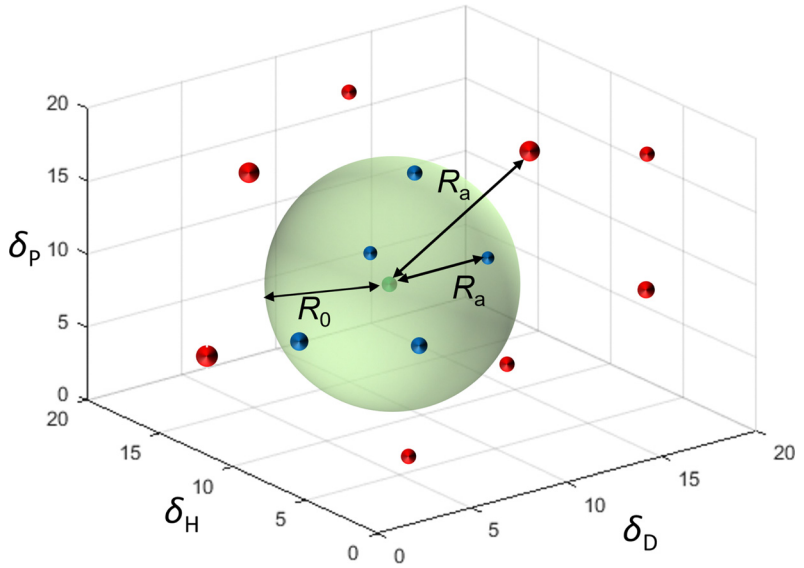

Fig. 2 Visualization of Hansen dissolution space with a biopolymer (green point) in the center of the sphere, chemicals predicted as solvents (blue points inside the sphere), chemicals predicted as non-solvent (red points outside of the sphere).

theory, which was previously described in paper by Vonka *et al.*[44] and (2) the PC-SAFT equation of state.

2.4.1 Flory–Huggins theory. The core of the model lies in the subsequent calculation of both binodal and spinodal points at different temperatures. In the Flory–Huggins model, the Gibbs free energy of mixing (ΔG_{mix}) the polymer (P)–solvent (S) system can be defined as

$$\frac{\Delta G_{mix}}{RT} = \frac{\phi_P \ln \phi_P}{N_P} + \frac{\phi_S \ln \phi_S}{N_S} + \phi_P \phi_S \chi \quad (5)$$

where R represents the universal gas constant, T is temperature, ϕ_i is volume fraction of the i-th component in the solution, N_i stands for the relative molecular size of component i, and χ is Flory–Huggins interaction parameter between polymer and solvent, which is estimated using well-known semi-empirical equation

$$\chi = \frac{V_S}{RT}(\delta_S - \delta_P)^2 + 0.34 \quad (6)$$

with δ_i being Hildebrand solubility parameter of component i and V_S molar volume of the solvent. The algorithm for phase diagram then proceeds as follows:

1. Temperature of the system is set close to its freezing point, *i.e.*, far from the critical temperature T_c, so that the

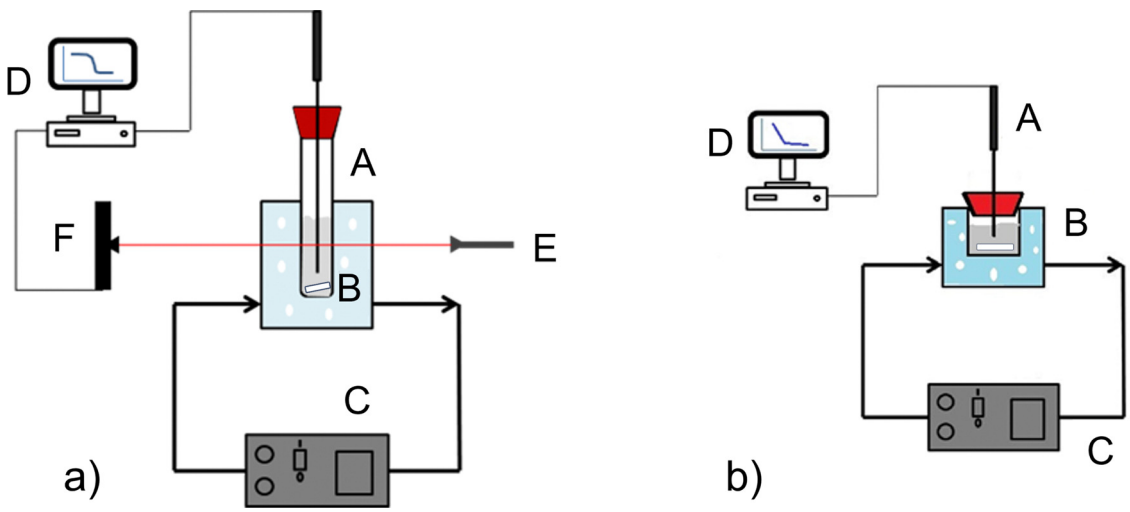

Fig. 3 (a) Cloud point measurement apparatus consisting of: A – glass test tube with magnetic stirrer and temperature sensor immersed in polymer solution, B – cooling bath, C – programmable thermostat with a cooling option, D – data collection system, E – laser source, F – photodetector, black box not visualized in the scheme; (b) freezing point measurement apparatus consisting of: A – temperature sensor immersed in polymer solution, B – double-layer glass cell with a cooling agent flowing through its walls and polymer solution with magnetic stirrer in the inner part, C, D being equivalent to (a). Partially adapted from.[43]

binodal points represented by volume fraction of polymer in polymer-lean ($\phi_{P,I}$) and polymer-rich ($\phi_{P,II}$) phase have a maximum possible distance from each other.

2. The binodal points $\phi_{P,I}$ and $\phi_{P,II}$ are found as part of numerical solution of four nonlinear equations representing (i) intersection of the $\Delta G_{mix}(\phi)$ curve, *cf.* eqn (5) with the tangent line that is common to both binodal points – eqn (7) and (8), (ii) slope of the tangent line at binodal points – eqn (9) and (10):

$$\Delta G_{mix}(\phi_{P,I}) = A\phi_{P,I} + B \quad (7)$$

$$\Delta G_{mix}(\phi_{P,II}) = A\phi_{P,II} + B \quad (8)$$

$$\frac{\partial \Delta G_{mix}(\phi_{P,I})}{\partial \phi} = A \quad (9)$$

$$\frac{\partial \Delta G_{mix}(\phi_{P,II})}{\partial \phi} = A \quad (10)$$

where part of the solution are also coefficients A and B representing the slope and intercept of the tangent line common to both binodal points.

3. Spinodal points $\phi_{P,spin,I}$ and $\phi_{P,spin,II}$ are subsequently calculated as inflection points on the $\Delta G_{mix}(\phi)$ curve, fulfilling the condition

$$\frac{\partial^2 \Delta G_{mix}(\phi_{P,spin,I})}{\partial \phi^2} = 0 \quad (11)$$

$$\frac{\partial^2 \Delta G_{mix}(\phi_{P,spin,II})}{\partial \phi^2} = 0 \quad (12)$$

where reasonably good initial guess for the solution of nonlinear eqn (11) and (12) is provided in the vicinity of the already known binodal points $\phi_{P,I}$ and $\phi_{P,II}$.

4. The system temperature is slightly increased, and the algorithm is repeated from step 2 until the critical temperature is reached. During the first loop iteration (*i.e.* at the lowest temperature), care must be taken to ensure that the numerical solution of eqn (7)–(10) converged to the physically realistic values of ϕ_P, which represent composition of two different phases, because the solution procedure is usually cumbersome, highly sensitive to the initial guess and often leading to the double-root $\phi_{P,I} = \phi_{P,II}$, for which two different phases cannot be distinguished.

A comparison of the model input parameter values that were used with their theoretical (literature-based) counterparts is presented in Table 3, where: δ_{lit}(T25) stands for Hildebrand parameter calculated from HSP[36,42] at 25 °C, δ(T0) stands for the value of Hildebrand parameter at the initial model temperature, and α stands for the thermal expansion coefficient. The higher value of δ(T0) for PCL, compared to literature, stems from its temperature dependence[37] incorporated into the model, where ΔT value in eqn (1)–(3) is negative for the temperature decrease from 25 °C to T0 and thus leads to higher δ value. This dependency would not exactly lead exactly to δ(T0) presented in Table 3, but some deviation from the literature can be expected due to differences in PCL molecular weight as well as dispersity $Đ$. The temperature dependence of MPTOL was not considered in order to decrease the complexity of the model. It is evident that the values used in the model are very close to the literature values, except for the relative molecular size of polymer (PCL) N_P, which was estimated to minimize deviation from experimental data – a common practice for thermodynamic models of this complexity.[44]

Table 3 Comparison of literature and computational parameters in the model based on Flory–Huggins lattice theory

Parameter	PCL	MPTOL
δ_{lit}(T25) (MPa$^{1/2}$)	20.3610	20.4375
δ(T0) (MPa$^{1/2}$)	23.2123	20.4375
α_{lit} (K^{-1})	1.6×10^{-4}	—
α (K^{-1})	1.6×10^{-4}	—
N_{teor}	492	1
N	16	1
V (cm^3 mol^{-1})	—	141.94

2.4.2 PC-SAFT equation of state. The PC-SAFT (Perturbed Chain-Statistical Associating Fluid Theory) equation of state was developed by J. Gross and G. Sadowski in 2001.[45] The model approximates molecules as chains of spherical segments that are free to move in space (unlike in the Flory–Huggins model, where the molecules are restricted to a regular lattice). The PC-SAFT model describes the residual Helmholtz energy (A^{res}) of a mixture as the sum of contributions:

$$A^{res}(T,V,N_i) = A^{hc} + A^{disp} + \ldots \quad (13)$$

where A^{hc} is the hard chain (repulsive) term and A^{disp} the contribution from dispersive (attractive) forces. The ellipsis indicates the possibility to add contributions from other types of interactions, such as dipole–dipole or hydrogen bonding interactions. Although the model is versatile, this adaptability creates confusion due to the variety of possible variants of the PC-SAFT equation of state. eqn (13) only includes the two terms used in our model.

The hard chain and dispersive terms are sufficient for the PCL-MPTOL system description using PC-SAFT model. Both molecules, except for the first and last PCL monomers, act as electron-pair donors and do not form hydrogen bonds. While incorporating dipole–dipole interactions could be appropriate, this leaves an unresolved issue for polymers, especially concerning the correct dipole moment value. The goal was to keep the PC-SAFT model as simple as possible by using the fewest parameters necessary.

The proposed PC-SAFT implementation employs the standard van der Waals mixing rules, which are grounded in the PC-SAFT theory. The pure components are described using three parameters with clear physical interpretation: the segment diameter (σ) the number of segments (m) and the energy parameter (ε). The pure component parameters used in this work are shown in Table 4.

The PCL parameters were taken from.[46] The MPTOL parameters, to the best of our knowledge, have not been reported in literature yet, therefore they were estimated using a group-contribution approach.[49] Unfortunately, the parameter set from

Table 4 PC-SAFT model pure component parameters

Substance	ε/k_B [K]	σ [Å]	m [—]	Ref.	Method
PCL	240.460	3.2746	0.037511 mol g^{-1} × M_w	46	Adjusted to pure density and binary LLE data.
Methyl-*p*-toluate	305.713	3.7400	3.937	Parameters optimized in this work, p_{sat}[47,48] MARD: 0.77% Density[48] MARD: 3.0%	Parameters optimized to match vapor pressures and density, initial estimate from GC method.[49]

the group-contribution method produced more than 4% mean absolute relative deviation (MARD) in vapor pressures of pure MPTOL. Therefore, these parameters were used only as an initial estimate and further optimized with respect to experimental vapor pressures in the range of 348 K to 407 K and MPTOL liquid density at 298 K. The optimized parameter values, MARD and experimental data references are summarized in Table 4.

The cross-pair parameters σ_{ij} and ε_{ij} were determined using the standard Lorentz–Berthelot combining rules:

$$\sigma_{ij} = \frac{1}{2}(\sigma_i + \sigma_j)(1 - l_{ij}) \quad (14)$$

$$\frac{\varepsilon_{ij}}{k_B} = \sqrt{\frac{\varepsilon_i}{k_B}\frac{\varepsilon_j}{k_B}}(1 - k_{ij}) \quad (15)$$

Here, k_{ij} is the cross-energy binary interaction parameter and l_{ij} is the cross-segment binary interaction parameter. Typically, k_{ij} is adjusted for each binary mixture to match experimental data, while k_{ij} set to zero represents a prediction based only on pure component parameters. l_{ij} corrects the size effects; in the current study, l_{ij} was set to zero, but the consequences of using it are discussed in the phase diagram section. To enhance reproducibility, the implementation of PC-SAFT was used in the form of open-source software package FeOs (version 0.7.0).[50]

The binodal points were calculated by solving the liquid–liquid equilibrium (LLE) using the direct Newton–Raphson numerical algorithm to solve for the isofugacity condition for each component:

$$\ln \varphi_i^{l1}(T,p,\boldsymbol{x}^{l1}) + \ln x_i^{l1} = \ln \varphi_i^{l2}(T,p,\boldsymbol{x}^{l2}) + \ln x_i^{l2} \quad (16)$$

2.4.3 Calculation of the solid–liquid equilibrium curve. The solid–liquid equilibrium (SLE) curve was derived from the thermodynamically exact equation for equilibrium between the pure crystalline MPTOL and the saturated liquid solution of MPTOL + PCL:

$$\ln\ \gamma_S(T,\boldsymbol{x}) + \ln\ x_S = -\frac{\Delta_{fus}h_S}{RT}\left(1 - \frac{T}{T_f}\right) + \int_{T_f}^{T}\Delta_{fus}c_{p,S}\mathrm{d}T + T\int_{T_f}^{T}\frac{\Delta_{fus}c_{p,S}}{T}\mathrm{d}T \quad (17)$$

In this equation, the parameters on the right-hand side depend only on pure MPTOL, $\Delta_{fus}h_S$ is the molar enthalpy of fusion and T_f is the melting temperature of pure MPTOL (Table 5). The last two terms depend on $\Delta_{fus}c_{p,S}$, which is the difference between the pure MPTOL molar isobaric heat capacities for the liquid and solid phases. It is common engineering practise to neglect the last two terms. The activity coefficient γ_S of the crystallizing substance in the binary mixture can be calculated using both presented thermodynamic models. With the PC-SAFT equation of state, existing procedures can be utilized for calculating fugacity coefficients and for calculating the ratio of fugacities in the mixture and in the pure component state:

$$\ln \gamma_i(T,\boldsymbol{x}) = \ln \varphi_i(T,p,\boldsymbol{x}) - \ln \varphi_i(T,p,\boldsymbol{x}_i = 1) \quad (18)$$

The Flory–Huggins theory provides an expression for the Gibbs energy of mixing; therefore, the expression for the activity coefficient can be directly derived (as a partial derivative of the excess Gibbs energy with respect to molar amount of i-th component), the resulting expression is as follows:

$$\ln \gamma_i(T,\boldsymbol{x}) = \ln \phi_i x_i + 1 - \phi_i x_i + \chi {\phi_2}^2 \quad (19)$$

The fugacity coefficient symbol φ_i is not to be confused with the volume fraction symbol ϕ_i used in other sections of this paper.

2.5 TIPS foaming procedure

An in-house built foaming vessel was used for sample preparation. The foaming vessel (*cf.* Fig. 4) consists of a stainless-steel vessel (D) with a screw and with a flange to attach bottom aluminium sheet (F). Between the top and the bottom part of the vessel, two O-rings (C, E) ensure the sealing. The vessel can be attached to a lyophilization apparatus *via* a stainless-steel top (A), which was not utilised as part of this work. This arrangement enables mostly one-dimensional heat transfer during the phase separation process due to the significantly more thermally conductive aluminium bottom sheet in comparison to the rest of the vessel made from the stainless-steel.[52] This design allows to avoid occurrence of voids and cracks in the samples, which can be caused by heat transfer taking place in more than one dimension.[53] A Teflon cylinder (B) can be used as an additional insulation. However, it significantly decreases the diameter of the samples and was not used in this work.

Table 5 SLE model parameters

Parameter	Methyl *p*-toluate	Ref.
T_f (K)	305	51
$\Delta_{fus}h_S$ (kJ mol^{-1})	20.78	51
$\Delta_{fus}c_{p,S}$ (J mol^{-1} K^{-1})	0.0 (approximation)	

The foaming procedure consisted of several steps: (1) a glass tube containing PCL pellets and 5 ml of methyl-*p*-toluate was placed into a preheated water bath kept at 70 °C to obtain a homogeneous and sufficiently fluid solution, that was subsequently poured into the foaming vessel preheated to 50 °C in order to prevent premature cooling and phase separation.

(2) The bottom sheet of the foaming vessel was immersed in the cooling bath, leading to a temperature quench to around −78.5 °C, the sublimation temperature of CO_2,[54] the cooling bath consisting of ethanol as the heat transfer liquid and dry ice as the cooling agent. This arrangement results in phase separation of PCL-MPTOL solution into polymer-rich and polymer-lean phases, and subsequent solidification after the system temperature decreases below the freezing temperature T_f.

(3) The frozen sample was transferred from the foaming vessel into a beaker with ethanol/methanol (96 : 4) mixture, acting as an extraction agent. The beaker was covered with a Petri dish and left at room temperature; implications of this are being further discussed in Section 3. Extraction led to the occurrence of two visually different liquid phases, and most of the extraction agent was exchanged once a day, while the extraction process was supported by occasional gentle beaker shaking, facilitating solution mixing. This process was repeated until the solution in the beaker stayed visually homogeneous, marking the end of the extraction process, after approximately 6 days.

(4) The sample was removed from the extraction agent and left to dry in a ventilated environment at room temperature.

2.6 Characterization methods

The molecular weight of the tested materials was measured using gel permeation chromatography (GPC). The analysis was conducted on an Agilent Technologies 1100 Series instrument (Santa Clara, CA, USA), equipped with an isocratic pump and an autosampler. A PLgel 5 μm mixed C column was maintained at 30 °C, using chloroform as the eluent at a flow rate of 1 mL min^{-1}. Linear polystyrene standards with narrow distribution were used to gain the calibration curve (9 points in calibration). The instrument was equipped with a refractive index detector.

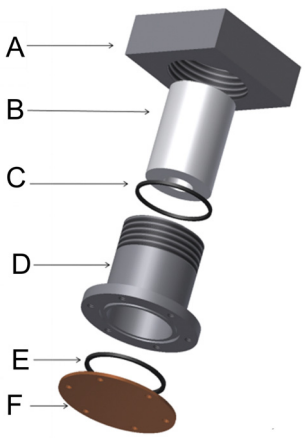

Fig. 4 Design of the foaming vessel. A – vessel top, B – insulating Teflon cylinder, C + E – sealing O-rings, D – stainless steel vessel, F – aluminium sheet. Partially adapted from Vonka *et al.*[44]

The morphology properties of the prepared samples were characterized by various methods. To visualize the structure of the samples, scanning electron Mmcroscopy (SEM) was employed. SEM was performed on VEGA 3 SBU, Tescan electron microscope, backscattered electron (BSE) mode, (high voltage) HV = 10–20 kV. All polymer samples have been coated with a layer of gold nanoparticles prior to SEM measurements.

Quantachrome PoreMaster 33 was employed to characterize the samples by low- and high-pressure mercury intrusion porosimetry (MIP) reaching pressure up to 414 MPa and allowing pore size determination in the range from 1.1 mm down to 6.4 nm. The results of mercury porosimetry are interpreted with caution due to risk of sample compression and ''bottleneck'' effect affecting the results.

3. Results and discussion

3.1 Dissolution experiments

PLA and PCL solvent candidates were identified using Hansen solubility theory as described in Section 2.1 for elevated temperature T_h = 80 °C, which was chosen as reasonably high to facilitate dissolution, and sufficiently low to avoid handling problems and other potential problems stemming from heating of chemicals. Value of R_0, influencing the size of dissolution sphere, was chosen to be equal to 10 $MPa^{1/2}$ in both cases to obtain enough of solvent candidates, while maintaining a reasonable probability of biopolymer dissolution. One set of HSP published by Bordes *et al.* was used as it was measured for PCL with M_w = 65 kDa, therefore with expectedly similar properties to the PCL, as defined by manufacturer, used in this study. On the contrary, due to lactic acid chirality and resulting significant differences in PLA, often insufficiently characterized by the producers in terms of chirality as well as molecular weight, four different sets of PLA HSP, taken from various sources,[38–41] were used in order to evaluate solvent candidates. Solvent candidates for each set of parameters, with $T_m \geq 0$, are listed in Supplement A, including the following information about the chemicals: HSP at 80 °C, melting temperature (T_m), boiling temperature (T_b), RED as well as RED at 80 °C, while toxicity and relative purchase cost at Sigma Aldrich (Merck) were indicated in three levels.

Chemicals exclusively in the lowest cost range, meaning <100 $ per 100 g, were chosen to be tested, if they were deemed to have sufficiently low toxicity, *i.e.*, either lowest toxicity level, as described in Section 2.1, or chosen chemicals pushed in mid-level due to danger to aquatic life, *cf.* Table 2. Dissolution experiments were conducted with solutions containing ~4 wt% of respective biopolymer (PLA6, PLA80 or PCL) at different temperatures while time to full homogenization was observed, *cf.* Table 7.

As expected, PCL tests were more successful due to the more precise HSP, with only one chemical out of 6 not dissolving and

others dissolving at 40 °C. Particularly promising, from the found PCL solvents, are: methyl *p*-toluate, ethyl cinnamate, and dimethyl phthalate. Ethyl cinnamate and dimethyl phthalate are very interesting solvents, particularly in the medical field, due to their low reported toxicity, *i.e.*, no hazard statements. However, their T_m are among the lowest out of the tested solvents and their PCL dissolution speed at given conditions was four times lower compared to methyl *p*-toluate (MPTOL), which exhibited the ability to quickly dissolve PCL, while having high T_m = 34 °C as well as a relatively low toxicity according to GHS statements,[29] *cf.* Table 2. Comparing acute oral toxicity to rats, MPTOL's lethal dosage LD50 = 3300 mg kg^{-1} [55] can be paralleled to a common table salt (NaCl) with LD50 = 3000 mg kg^{-1}.[56] It is classified by European Chemical Agency (ECHA) as a readily biodegradable compound and is not bioaccumulative, mutagenic nor teratogenic based on conducted studies.[29] Albeit its lack of comprehensive toxicology tests in tissue engineering field, due to its primary prior uses lying in the field of organic synthesis and fragrance product such as soaps,[55] current level of toxicity knowledge implies its application potential in both membranes and tissue engineering. Therefore, out of the novel solvents presented in Table 7, methyl *p*-toluate in combination with PCL was chosen to be studied further.

Both PLA6 and PLA80 were dissolved by 5 of the 15 tested chemicals at higher temperatures when compared to PCL. A comparatively lower success rate in the case of PLA was attributed to the purposeful choice of variety of HSP explained above, as ideally only one set of parameters should be used for one polymer. The most promising out of the presented PLA solvents is acetophenone with T_m = 19.5 °C, relatively low toxicity reported, and particularly fast dissolution of PLA6. Moreover, although acetophenone has a low water solubility, it is freely soluble in ethanol, which could be used as a low-cost, low-toxicity extraction agent in the last step of TIPS.[29]

To further define biopolymers used, GPC measurement was utilized. Values of obtained number- and weight-average molecular weights M_n, M_w and dispersity $Đ$ of polymer samples are summarized in Table 6. In the case of PCL, values before and after the TIPS are presented as well.

3.2 Phase diagram

To further study the novel PCL/MPTOL system, a phase diagram was constructed using the experimental approach aided by computational modelling, *cf.* Fig. 5. Time demanding experimental measurements were done at a temperature decrease rate of 0.3 °C min^{-1} for cloud points as well as freezing points and at least three measurements were averaged for each data point presented in Fig. 5.

The cloud points were used to adjust parameters of a computational model based on Flory–Huggins lattice theory, which supplied the phase diagram in Fig. 5 with a binodal curve and a thermodynamically coupled spinodal curve. The parameters used in the computational model, described in Section 2.4, were in good agreement with literature data for a thermodynamic model of this complexity.[44] Simple linear regression was used to indicate a decreasing trend in the freezing point data. Five PCL concentrations were chosen, *cf.* Fig. 5, for TIPS experiments to further validate the phase diagram and to study the influence of initial solution concentration on the final foam morphology.

To further validate the binodal curves calculated by the Flory–Huggins model, the LLE calculation was performed with the PC-SAFT equation of state. LLE prediction is generally very sensitive to the energy parameter ε and with the PC-SAFT equation of state, it is necessary to adjust the binary interaction parameter k_{ij} to yield reasonable results. Interestingly, it was not possible to reproduce the experimental points solely by adjusting the cross energy binary interaction parameter k_{ij}, the binodal curve was still shifted to the left. This indicated that the model's deficiency lies in the differences in the size and shape of the molecules (entropic effects) rather than in the energetic interactions. Moreover, the Flory–Huggins model assumes that PCL is only approximately 16 times larger than a molecule of MPTOL, therefore a similar approach in the PC-SAFT model was assumed, and the molecule of PCL was shortened from $M_{nPCL\text{-}GPC}$ = 20.2 kg mol^{-1} to 1.5 kg mol^{-1}. An alternative approach to correct the entropic deficiencies of the model would be to adjust the cross-segment interaction parameter l_{ij}, however, to maintain simplicity, it was decided not to utilize the second interaction parameter. The resulting binodal curve is displayed in Fig. 6. It is evident that the results of both Flory–Huggins (Fig. 5) and PC-SAFT (Fig. 6) model predictions can render the experimental data quite well, raising question about the possible change of PCL molecular weight after dissolution in MPTOL. To examine the potential decrease in molecular chain length, the final PCL molecular weight in prepared porous materials was measured using GPC to be: $M_{nPCL\text{-}end}$ = 36.6 kg mol^{-1}; $M_{wPCL\text{-}end}$ = 124.1 kg mol^{-1}; $Đ_{PCL\text{-}end}$ = 3.4; *i.e.* the complete TIPS process led to significant increase in M_n and slight decrease in M_w of PCL, *cf.* Table 6. Therefore, no significant decrease in polymer chain length was observed, while increase in M_n can be explained by extraction of shorter polymer chains during the solvent removal.

Additionally, the PC-SAFT model approach allowed calculation of SLE equilibria of crystalline MPTOL, *cf.* Fig. 6. The calculations are in agreement with literature data regarding MPTOLs T_m,[58] which is, interestingly, notably higher than our measurement of the systems T_f, *cf.* Fig. 1 and 5. The difference between solidification and melting temperature is advantageous for application in TIPS as, despite T_f values reaching below 0 °C, extraction part of the process can be maintained at room temperature. The presented SLE equilibria can be

Table 6 GPC molecular weight measurement results of used biopolymers with calculated dispersity $Đ_{GPC} = M_{w\text{-}GPC}/M_{n\text{-}GPC}$

	$M_{w\text{-}GPC}$ (kg mol^{-1})	$M_{n\text{-}GPC}$ (kg mol^{-1})	$Đ_{GPC}$ (—)
PLA6	138.6	28.7	4.8
PLA80	79.9	23.1	3.5
PCL	131.3	20.2	6.5
PCL_{end}	124.1	36.6	3.4

Table 7 Results of dissolution tests conducted with biopolymers and solvents suggested by Hansen solubility theory; T_m – solvent melting temperature; T_b – solvent boiling temperature; p_{triple} – triple point pressure; T_{dmin} – minimal tested homogenization temperature; t_d – time until homogenization; X (*x*) – not homogenized at maximal tested temperature (*x*)

					PLA6		PLA80	PCL	
Solvent	T_m (°C)	T_b (°C)	p_{triple} (Pa)	Ref.	T_{dmin} (°C)	t_d (h)	t_d (h)	T_{dmin} (°C)	t_d (h)
o-Bromoanisole	1.3	216.0	0.66	57,58	80	12	18	—	—
p-Bromotoluene	26.8	184.4	142.96	58	130	3	0.5	—	—
Benzoic acid	122.4	249.1	806.79	58,59	130	1	1.5	—	—
Acetophenone	19.5	202.1	30.93	58	80	0.5	4	—	—
trans-Anethole	22.2	235.5	6.54	58,60	130	3	1.5	40	1.5
Methyl *p*-toluate	34.0	218.5	31.60	58,61	X(80)	—	—	40	1.5
Ethyl cinnamate	6.0	271.0	0.26	57,58	X(80)	—	—	40	6
Dibenzyl ether	3.6	288.3	0.01	58,62	X(80)	—	—	40	6
Dimethyl phthalate	1.0	283.7	0.02	58,62	X(80)	—	—	40	6
1-Decanol	6.8	231.0	0.18	58	X(80)	—	—	X(40)	—
2,4-Dichlorobenzaldehyde	71.0	233	65.53	57,58	X(80)	—	—	—	—
4′-Methoxyacetophenone	37.5	255	4.86	58,63	X(80)	—	—	—	—
p-Chlorobenzoyl chloride	16	246.7	1.10	35,58	X(80)	—	—	—	—
4-Bromophenetole	4	230.9	—	35,60	X(80)	—	—	—	—
4-Chloro-2-nitrotoluene	36.5	266.4	20.65	58	X(80)	—	—	—	—

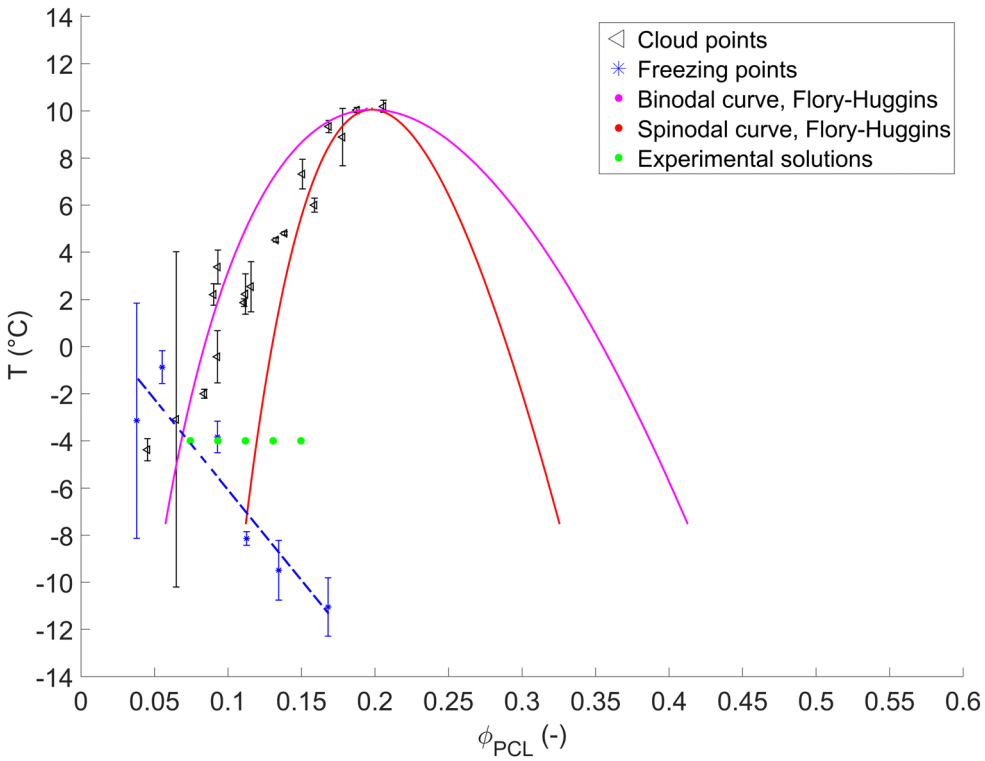

Fig. 5 Phase diagram of PCL/MPTOL system, consisting of experimentally determined cloud points and freezing points supplemented by binodal and spinodal curves constructed using computational model based on Flory–Huggins lattice theory and further supplemented by linear extrapolation used to better visualize trend in freezing points data.

therefore thought of as maximum TIPS solvent extraction temperature.

The properties of the PCL/MPTOL system make MPTOL similarly or even less energetically demanding TIPS solvent in comparison to the toxic solvents commonly used in literature. Although the first step of homogenization might be several hours longer compared to the TIPS process reported by Ujčić *et al.*,[64] who used 1,4-dioxane to dissolve PCL, the rest of the reported process includes cooling the system to −18 °C for 24 h, and the subsequent highly energetically demanding solvent removal by freeze-drying for 24 h at −55 °C. In comparison, PCL/MPTOL system similarly allows temperature quench to −15 °C and below but leads to cooling energy cost reduction during solvent removal by extraction at room temperature allowed by MPTOL's high T_m.

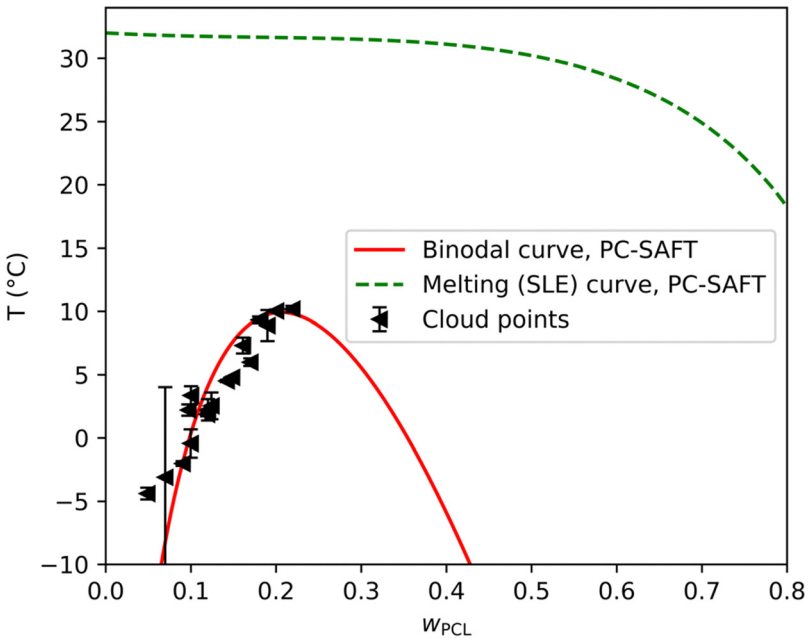

Fig. 6 Phase diagram of PCL/MPTOL system, consisting of experimentally determined cloud points supplemented by binodal (solid) and SLE (dashed) curve calculated by the PC-SAFT equation of state, M_w(PCL) = 1500 g mol^{-1} and k_{ij} = 0.022.

3.3 Structure visualization

The morphology of foams prepared by TIPS can be mainly influenced by two factors: (a) cooling rate, and (b) composition of polymer solution, in this work the focus is on the latter. The influence of the PCL concentration in MPTOL was qualitatively studied using five different solution concentrations, *cf.* Fig. 5, starting with 8 wt% of PCL, increased by 2% increment, up to 16 PCL wt%. Samples, with height ≈5 mm were cut prior to the SEM characterization to enable visualization of the bulk structure. To minimize potential structure alterations, the foams were cooled by liquid nitrogen prior to being cut by a surgical knife. Cuts from the middle of the sample were used to show the structure developed without influence of the horizontal heat transfer through the foaming vessel walls.

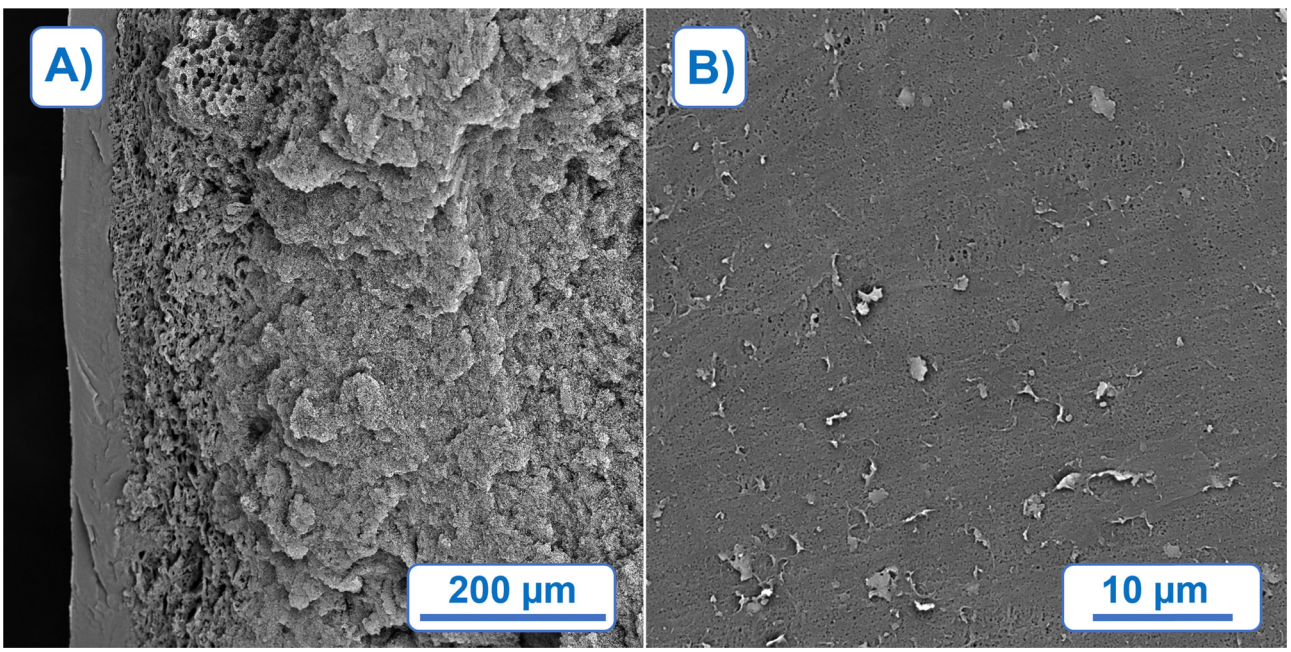

Fig. 7 SEM morphology visualization of PCL foam, prepared by TIPS from PCL/MPTOL solution containing 16 PCL wt%, containing: (A) cross-section near the bottom of the sample, (B) bottom surface, defined as the side in contact with the cooling plate.

Spatial differences were observed, *cf.* Fig. 7(A), with the smallest pores and the densest structure formed near the cooling plate, visible on the left side of Fig. 7(A), in approximately first 60 μm. Such changes are typical for TIPS due to the thermal gradient present during the quenching process, *i.e.* shorter de-mixing time near the cooling plate. Visualization of surface in contact with the cooling plate, *cf.* Fig. 7(B), indicates sufficiently small pores for the application potential in the membrane field.

The influence of polymer concentration on bulk morphology was assessed using cross-section cuts in a distance of ≈0.5 mm from the cooling plate. A distinct influence of solution concentration on the final morphology, typical for TIPS, was observed in the chosen concentration range, *cf.* Fig. 8. By comparing the bottom part of Fig. 8 three distinct morphologies can be discerned, from left to right: (1) flaky interconnected morphology, (2) dual morphology character with large pore globules partially interconnected by walls with smaller pores, and (3) uniformly interconnected porous structure. The first morphology type indicates phase separation exclusively in meta-stable region, a region between binodal curve and spinodal curve in a phase diagram. The second type indicates combination of de-mixing processes present in meta-stable and unstable region. Larger globules can be attributed to Ostwald ripening and coalescence in the meta-stable region, while smaller partially interconnected pores between globules can be attributed to spinodal decomposition taking place at the end of the process, after reaching the unstable region. The third and the last observed type can be attributed to the prevalent effect of spinodal decomposition, while partial non-homogeneity of the structure can be attributed to the minor effects of meta-stable de-mixing mechanisms.

Our morphology-related findings are in a good agreement with the presented phase diagram, *cf.* Fig. 5, as polymer solutions leading to the first type lie exclusively in the meta-stable region, the second type of morphology was observed for solutions going through both the meta-stable and unstable region, while the last solution separated, according to the phase diagram, almost exclusively by spinodal decomposition.

As homogeneity is one of the common requirements in various applications, the third morphology type is the most promising regarding application in membranes and tissue engineering, *i.e.* PCL wt% of 16 and above with pore size controlled *via* cooling conditions based on specific needs of the target application. On the other hand, the second morphology type could be utilized in more niche applications such as supported liquid membranes.[65] The first morphology type could be used in controlled drug delivery applications[66] provided that a sufficiently high initial polymer concentration is used in order to retain mechanical stability of the material.

3.4 Quantitative morphology characterization

Based on the qualitative results and the primary focus of this study on applications with interconnected structure as well as

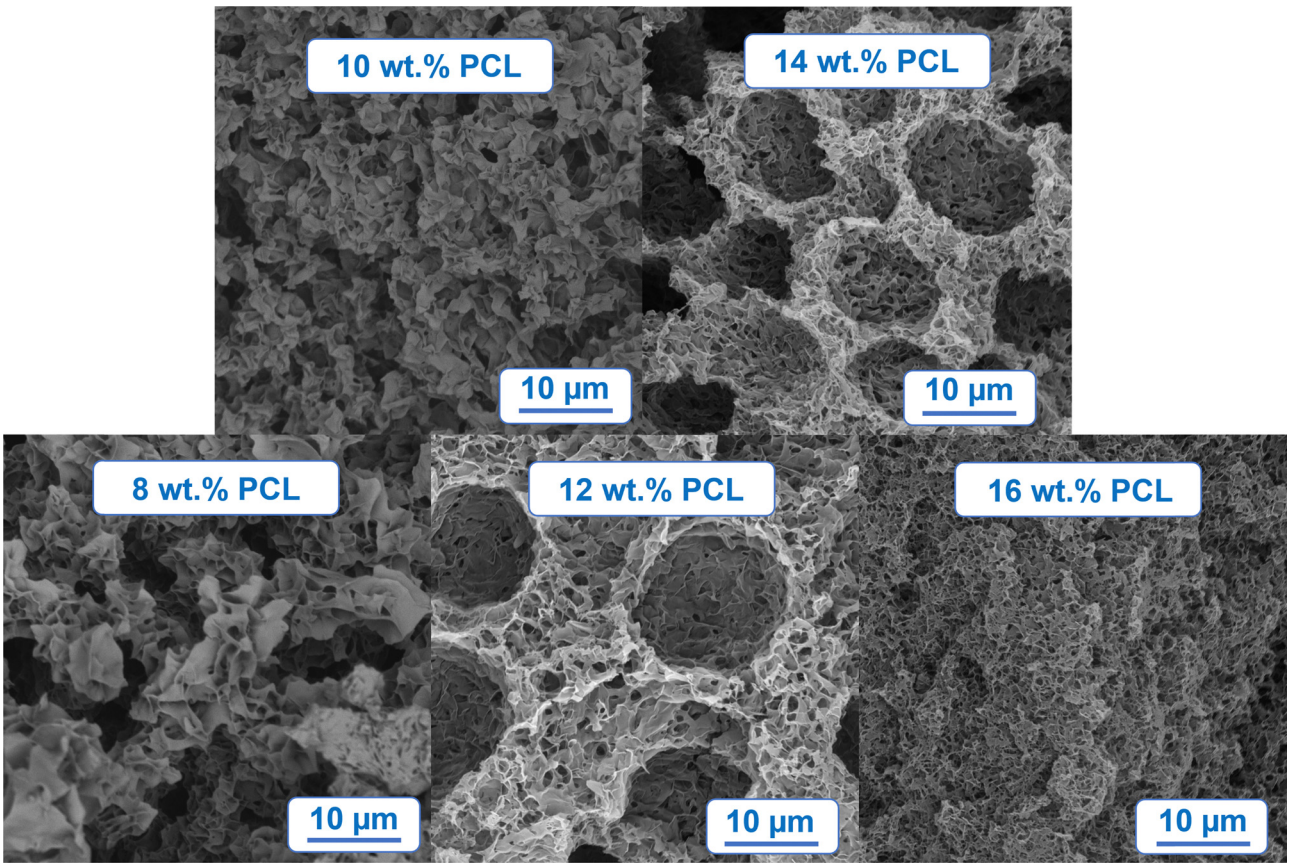

Fig. 8 SEM morphology visualization of PCL foam prepared by TIPS from PCL/MPTOL solutions containing 8, 10, 12, 14 and 16 PCL wt%.

good mechanical properties for membranes and scaffolds, the foams born from solutions with higher polymer content of 12, 14, and 16 PCL wt%, hence called 12PCL, 14PCL, and 16PCL, were studied in greater detail using MIP, allowing a quantitative comparison of pore size distribution (*cf.* Fig. 9), porosity and total pore surface area (*cf.* Fig. 12). Sample cuts for MIP were taken from the centre of nitrogen cooled samples, while the presented results were averaged from measurements of three samples per each tested concentration. Majority of the pore volume, *cf.* Fig. 9, was measured below the size of 10 μm (77.2%, 84.1%, 83.7%, respectively), and more than 95% of pore volume was measured below 100 μm (96.2%, 97.0%, 96.9%, respectively).

As evident from the comparison of Fig. 9 and 10, the pore size distribution is considerably moved towards lower values considering pore frequency in contrast to volume percentage. More than 99.5% of pores was measured to be smaller than 1 μm in all cases (99.6%, 99.7%, 99.6%, respectively). A similar number of pores was located below 50 nm for 12PCL and 16PCL (70.0% and 70.7%, respectively) with only 56% of pores for 14PCL. The highest number of pores below 10 nm measured for 12PCL can be attributed to the influence of solvent removal by extraction agent, leading to partial shrinkage and pore size decrease more prominent at lower polymer concentrations, as previously reported by Boura *et al.*[17] However, based on qualitative measurement, the MIP results can be skewed towards lower values for 12PCL and 14PCL, due to their dual morphology character potentially leading to a bottleneck effect.

The lowest measured average pore size was 58.1 nm for 12PCL, followed by 64.1 nm for 16PCL and 99 nm for 14PCL, *cf.* Fig. 11. Such values are better suited for membranes in comparison to scaffold applications, which require larger pore sizes in the order of tens or hundreds of microns.[67] Nevertheless, pore sizes tailored for specific cells or tissues should be achievable by cooling procedure alteration, *i.e.*, giving the system more time to separate by spinodal decomposition resulting in larger pore sizes.[68] Simultaneously, smaller pore sizes should be achievable by faster cooling and making the samples sufficiently thin for membrane applications.

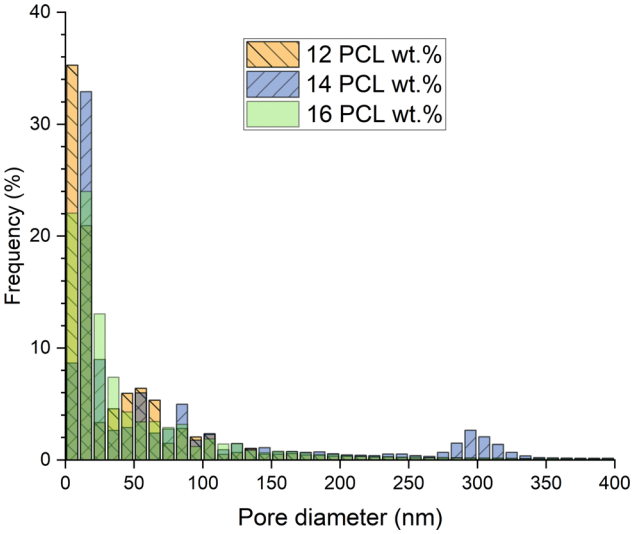

Fig. 10 Pore frequency distribution comparison of samples prepared from PCL/MPTOL solutions containing 12, 14, and 16 wt% of PCL. Measured by MIP and visualized in fractions of 10 nm.

In comparison, smaller average pore sizes, *cf.* Fig. 11, were obtained than the values reported by Manholi *et al.*[69] who utilized NIPS to prepare PCL membranes while using commonly used toxic solvents such as THF (369.7 nm) or 1,4-dioxane (120.4 nm).

The measured porosity, *cf.* Fig. 12, is promising for both membranes and tissue engineering applications based on results presented in the literature.[67,70] A slight increase in porosity with polymer concentration was observed, with 71.8% for 12PCL, 72.7% for 14PCL and 74% for 16PCL, which can be attributed to the

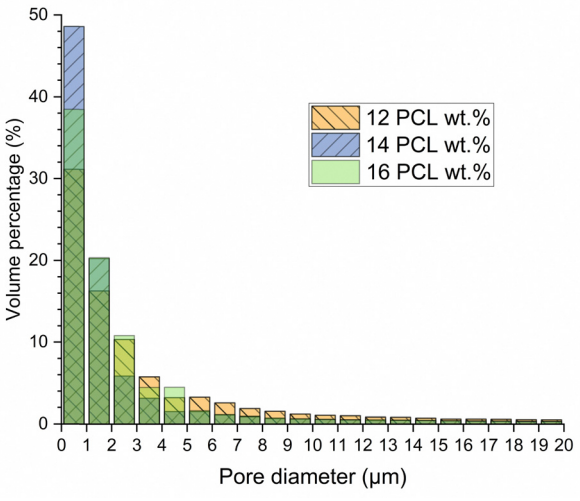

Fig. 9 Pore size distribution comparison of samples prepared from PCL/MPTOL solutions containing 12, 14, and 16 wt% of PCL. Measured by MIP and visualized in micron increments.

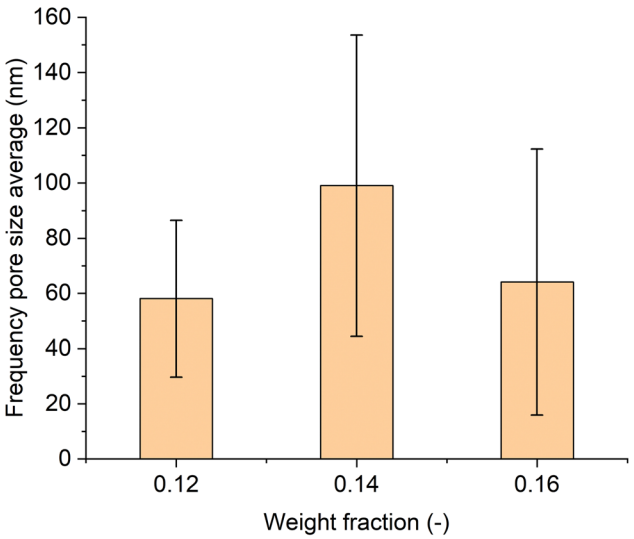

Fig. 11 Average pore size of samples, based on pore frequency, prepared from PCL/MPTOL solutions containing 12, 14, and 16 wt% of PCL. Measured by MIP.

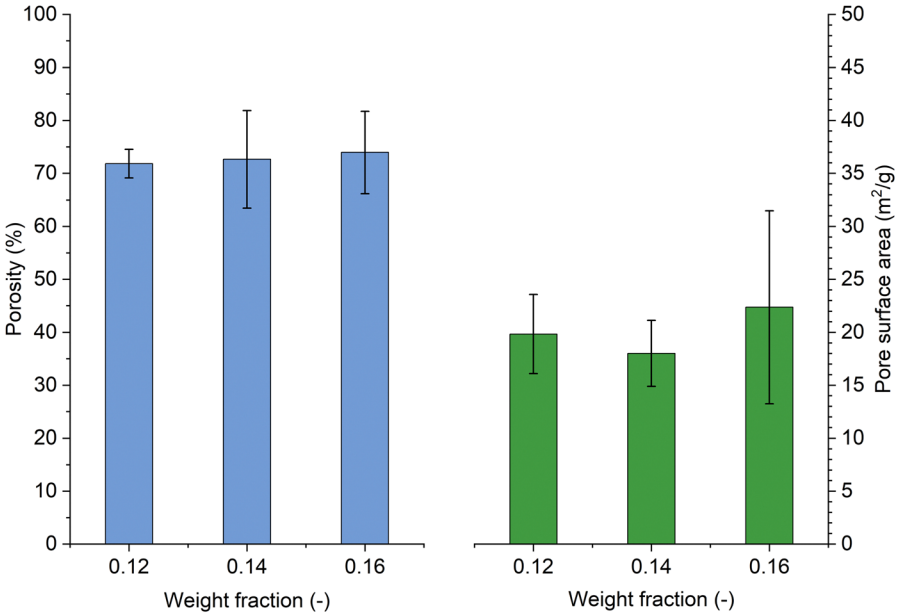

Fig. 12 Porosity and pore surface area comparison of samples prepared from PCL/MPTOL solutions containing 12, 14, and 16 wt% of PCL. Measured by MIP.

higher solvent removal shrinkage resistance with increasing polymer concentration.[17] The average pore surface area calculated from MIP data exceeded 15 $m^2\ g^{-1}$ in all cases with no significant trend observed, *cf.* Fig. 12.

4. Conclusions

Several novel, high melting point, low-toxicity and low-cost, PLA and PCL solvents were discovered by using Hansen solubility theory and screening of 846 chemicals in combination with subsequent experimental validation. The presented solvents could serve as a less toxic alternative to other chemicals currently used for not only thermally induced phase separation (TIPS), but phase separation in general, while retaining or improving the economic viability of the process due to their high T_m and reasonable purchase costs.

A particularly promising system was found with PCL dissolved in methyl *p*-toluate (MPTOL). This system was further investigated by constructing a phase diagram based on experimental measurements of cloud points and freezing points, supplemented by computational modelling, using a model based on Flory–Huggins theory and a PC-SAFT equation of state. PCL dissolved in MPTOL proved to be a promising TIPS combination due to the cloud points as well as freezing points being below MPTOL $T_m \approx 34$ °C implying the possibility of solution homogenization at relatively low temperature together with solvent removal at room temperature, which could significantly reduce the energy costs related to the TIPS process.

Using the PCL/MPTOL system and the ethanol/methanol (96/4) mixture as the extraction agent at room temperature, PCL foams with gradient morphologies were successfully prepared *via* TIPS. With increasing PCL wt%, three different morphology types were observed: (1) flaky interconnected morphology, (2) dual morphology character with big pore globules partially interconnected by walls with smaller, and (3) uniformly interconnected porous structure. The observed morphologies thermodynamically conform to the presented phase diagrams, with the first type occurring in the meta-stable region, the second one developing in both meta-stable and unstable region, and with the last one occurring in the unstable region due to the prevalence of spinodal decomposition.

Qualitatively compared foams had a porosity slightly above 70%, while exhibiting a minor porosity increase with increasing PCL concentration, and pore sizes averaging below 100 nm. By altering the TIPS process parameters, smaller as well as larger pore sizes can be achieved, to prepare materials with tailored properties. This flexibility, together with the option of method combination, leads to various application possibilities of the novel PCL/MPTOL system, particularly in membrane technology and tissue engineering.

Author contributions

Patrik Boura: writing – original draft, investigation, formal analysis, validation, methodology, data curation, software. Lenka Krajakova: investigation, validation, methodology, writing – review & editing. Adam Bouz: writing – original draft, formal analysis, methodology, software. Silvestr Figalla: investigation, resources, writing – review & editing. Alexandr Zubov: supervision, project administration, writing – original draft, writing – review & editing, software. Bart Van der Bruggen: supervision, conceptualization, writing – review & editing. Juraj Kosek: project administration, supervision, funding acquisition, writing – review & editing, resources, conceptualization.

Data availability

The authors confirm that the data supporting the findings of this study are available within the article and its ESI,† while additional raw measurement data can be provided by corresponding author upon request.

Conflicts of interest

The authors declare that they have no known competing financial interests or personal relationships that could have appeared to influence the work reported in this paper.

Acknowledgements

The support of Specific university research – grants no. A2_FCHI_2021_04, A2_FCHI_2023_036, and A1_FCHI_2024_004 is acknowledged.

References

1 M. Cavo and S. Scaglione, *Mater. Sci. Eng., C*, 2016, **68**, 872–879.
2 T. Defang, Z. Tienan, X. Yuanqiang, Z. Xiaomin and Z. Yongchun, *Sep. Purif. Technol.*, 2021, **263**, 118393.
3 Q. Yao, K. E. Fuglsby, X. Zheng and H. Sun, *J. Mater. Chem. B*, 2020, **8**, 3842–3851.
4 S. Tarafder, W. S. Dernell, A. Bandyopadhyay and S. Bose, *J. Biomed. Mater. Res., Part B*, 2015, **103**, 679–690.
5 Y. C. Wu, N. Zhang, G. Yuen and C. F. de Lannoy, *Chem. Eng. J.*, 2023, **455**, 12.
6 S. H. Y. Hong, F. Al Marzooqi, J. K. El-Demellawi, N. Al Marzooqi, H. A. Arafat and H. N. Alshareef, *ACS Mater. Lett.*, 2023, **5**, 341–356.
7 O. Georg, F. M. Elise, J. S. Sandra, K. Lamya, M. M. Laoise and A. Peter, *Injury*, 2016, **47**, S11–S20.
8 H. Qu, W. Zhang, Z. Li, L. Hou, G. Li, J. Y. H. Fuh and W. Wu, *Int. J. Precis. Eng. Manuf.*, 2022, **23**, 689–699.
9 X. Feng, P. Xu, T. Shen, Y. Zhang, J. Ye and C. Gao, *J. Mater. Chem. B*, 2020, **8**, 391–405.
10 Y. J. Hou, X. Y. Wang, J. Yang, R. Zhu, Z. R. Zhang and Y. Li, *J. Biomed. Mater. Res., Part A*, 2018, **106**, 1288–1298.
11 P. R. Gabbai-Armelin, M. T. Souza, H. W. Kido, C. R. Tim, P. S. Bossini, K. R. Fernandes, A. M. P. Magri, N. A. Parizotto, K. P. S. Fernandes, R. A. Mesquita-Ferrari, D. A. Ribeiro, E. D. Zanotto, O. Peitl and A. C. M. Renno, *J. Tissue Eng. Regener. Med.*, 2017, **11**, 1141–1151.
12 J. Shao, S. Chen and C. Du, *J. Mater. Chem. B*, 2015, **3**, 5291–5299.
13 F. Asghari, M. Samiei, K. Adibkia, A. Akbarzadeh and S. Davaran, *Artif. Cells, Nanomed., Biotechnol.*, 2017, **45**, 185–192.
14 D. Y. Mao, Q. Li, D. K. Li, Y. S. Chen, X. H. Chen and X. Xu, *Mater. Des.*, 2018, **142**, 1–10.
15 J. W. Jang, K. E. Min, C. Kim, J. Shin, J. Lee and S. Yi, *Int. J. Precis. Eng. Manuf.*, 2023, **24**, 511–529.
16 J. F. Kim, J. H. Kim, Y. M. Lee and E. Drioli, *AIChE J.*, 2016, **62**, 461–490.
17 P. Boura, A. Zubov, B. Van der Bruggen and J. Kosek, *J. Porous Mater.*, 2024, **31**, 1425–1435.
18 H. Matsuyama, S. Kudari, H. Kiyofuji and Y. Kitamura, *J. Appl. Polym. Sci.*, 2000, **76**, 1028–1036.
19 C. A. Martinez-Perez, I. Olivas-Armendariz, J. S. Castro-Carmona and P. E. Garcia-Casillas, *Scaffolds for Tissue Engineering Via Thermally Induced Phase Separation*, Intech Europe, Rijeka, 2011.
20 C. Y. Gao, A. Li, L. X. Feng, X. S. Yi and J. C. Shen, *Polym. Int.*, 2000, **49**, 323–328.
21 V. La Carrubba, F. C. Pavia, V. Brucato and S. Piccarolo, *Int. J. Mater. Form.*, 2008, **1**, 619–622.
22 S. Gay, G. Lefebvre, M. Bonnin, B. Nottelet, F. Boury, A. Gibaud and B. Calvignac, *J. Supercrit. Fluids*, 2018, **136**, 123–135.
23 F. Carfì Pavia, V. La Carrubba and V. Brucato, *Polym. Bull.*, 2013, **70**, 563–578.
24 Y. Wang, J. Dai, Q. Zhang, Y. Xiao and M. Lang, *Appl. Surf. Sci.*, 2010, **256**, 6107–6112.
25 M. Wang, L. Ma, D. Li, P. Jiang and C. Gao, *J. Biomed. Mater. Res., Part A*, 2013, **101**, 3219–3227.
26 V. Guarino, A. Guaccio, D. Guarnieri, P. A. Netti and L. Ambrosio, *J. Biomater. Appl.*, 2012, **27**, 241–254.
27 C. Schugens, V. Maquet, C. Grandfils, R. Jerome and P. Teyssie, *Polymer*, 1996, **37**, 1027–1038.
28 N. P. Cheremisinoff, John Wiley & Sons, **https://app.knovel.com/hotlink/toc/id:kpGRAPGEE1/groundwater-remediation/groundwater-remediation**, (Accessed 15th July 2024).
29 E. C. Agency, European Chemicals Agency, **https://echa.europa.eu/**, (accessed 9th November, 2024).
30 J. G. Speight John Wiley & Sons, **https://app.knovel.com/hotlink/toc/id:kpRTPE0002/rules-thumb-petroleum/rules-thumb-petroleum**, (Accessed 15th July 2024).
31 Ö. C. Önder, E. Yilgör and I. Yilgör, *Polymer*, 2016, **107**, 240–248.
32 *CRC Handbook of Chemistry and Physics*, CRC Press, 97th edn.
33 M. Verheijen, M. Lienhard, Y. Schrooders, O. Clayton, R. Nudischer, S. Boerno, B. Timmermann, N. Selevsek, R. Schlapbach, H. Gmuender, S. Gotta, J. Geraedts, R. Herwig, J. Kleinjans and F. Caiment, *Sci. Rep.*, 2019, **9**, 4641.
34 A. Salerno and C. Domingo, *J. Porous Mater.*, 2015, **22**, 425–435.
35 C. L. Yaws Yaws' Thermophysical Properties of Chemicals and Hydrocarbons (Electronic Edition), Knovel, **https://app.knovel.com/hotlink/toc/id:kpYTPCHE02/yaws-thermophysical-properties/yaws-thermophysical-properties**, (Accessed 15th July 2024).
36 C. M. Hansen, *Hansen Solubility Parameters: A User's Handbook*, Crc Press, 1st edn, 1999.
37 C. M. Hansen, *Hansen solubility parameters: A user's handbook*, CRC Press, Boca Raton, Fla., 2nd edn, 2007.
38 C. Hansen, https://www.hansen-solubility.com/HSP-science/sphere.php, (accessed 10th June, 2024).
39 K. Adamska, A. Voelkel and A. Berlińska, *J. Pharm. Biomed. Anal.*, 2016, **127**, 202–206.

40 M. Esmaeili, G. Pircheraghi, R. Bagheri and V. Altstädt, *Polym. Adv. Technol.*, 2019, **30**, 839–851.
41 R. A. Auras, L. T. Lim, S. E. M. Selke and H. Tsuji, *Poly(lactic acid): Synthesis, Structures, Properties, Processing, and Applications*, Wiley, 2011.
42 C. Bordes, V. Fréville, E. Ruffin, P. Marote, J. Y. Gauvrit, S. Briançon and P. Lantéri, *Int. J. Pharm.*, 2010, **383**, 236–243.
43 A. Nistor, M. Vonka, A. Rygl, M. Voclova, M. Minichova and J. Kosek, *Macromol. React. Eng.*, 2017, **11**, 1600007.
44 M. Vonka, A. Nistor, A. Rygl, M. Toulec and J. Kosek, *Chem. Eng. J.*, 2016, **284**, 357–371.
45 J. Gross and G. Sadowski, *Ind. Eng. Chem. Res.*, 2001, **40**, 1244–1260.
46 I. Ushiki, H. Kawashima, S.-I. Kihara and S. Takishima, *J. Supercrit. Fluids*, 2022, **181**, 105499.
47 A. R. R. P. Almeida and M. J. S. Monte, *J. Chem. Eng. Data*, 2011, **56**, 4862–4867.
48 B. Semeniuk and H. Wilczura-Wachnik, *Fluid Phase Equilib.*, 1998, **152**, 337–345.
49 E. Sauer, M. Stavrou and J. Gross, *Ind. Eng. Chem. Res.*, 2014, **53**, 14854–14864.
50 P. Rehner, G. Bauer and J. Gross, *Ind. Eng. Chem. Res.*, 2023, **62**, 5347–5357.
51 A. V. Blokhin, Y. U. Paulechka, G. J. Kabo and A. A. Kozyro, *J. Chem. Thermodyn.*, 2002, **34**, 29–55.
52 LLC., Thermal Properties of Metals, Conductivity, Thermal Expansion, Specific Heat – Engineers Edge, **https://www.engineersedge.com/properties_of_metals.htm**, (accessed 15th March, 2024).
53 J. H. Aubert and R. L. Clough, *Polymer*, 1985, **26**, 2047–2054.
54 C. R. Barber, *Br. J. Appl. Phys.*, 1966, **17**, 391–397.
55 N. C. f. B. Information, PubChem Substance Record for SID 134972054, Methyl 4-methylbenzoate, **https://pubchem.ncbi.nlm.nih.gov/substance/134972054**, (accessed 9th November, 2024).
56 D. B. Hipgrave, S. Chang, X. Li and Y. Wu, *JAMA*, 2016, **315**, 703–705.
57 Table 2. Physical Properties – Organic Compounds, **https://app.knovel.com/hotlink/itble/rcid:kpYCPDCECD/id:kt009ZN2I4/yaws-critical-property/table-2-physical-properties**, (Accessed 15th July 2024).
58 C. D. M. A. Y. S. A. B. R. D. C. J. W. M. Y. P. A. F. K. S. A. T. E. W. L. M. Vladimir Diky NIST/Thermodynamics Research Center (TRC), **https://app.knovel.com/hotlink/toc/id:kpNISTSRD3/nist-standard-reference/nist-standard-reference**, (Accessed 15th July 2024).
59 Interactive Table of Physical, Health and Safety Properties, **https://app.knovel.com/hotlink/itble/rcid:kpSHPACE01/id:kt00CYZQL2/sittigs-handbook-pesticides/interactive-table-physical**, (Accessed 15th July 2024).
60 Basic Physical Properties of Chemical Compounds, **https://app.knovel.com/hotlink/itble/rcid:kpKCTE000X/id:kt002VLXT1/knovel-critical-tables/basic-physical-properties**, (Accessed 15th July 2024).
61 Basic Physical Properties of Chemical Compounds, **https://app.knovel.com/hotlink/itble/rcid:kpKCTE000X/id:kt002VLXT1/knovel-critical-tables/basic-physical-properties**, (Accessed 15th July 2024).
62 Critical Properties and Acentric Factors - Organic Compounds, **https://app.knovel.com/hotlink/itble/rcid:kpYTPCHE02/id:kt0078-OO11/yaws-thermophysical-properties/yaws-therm-critical-properties**, (Accessed 15th July 2024).
63 Basic Physical Properties of Chemical Compounds, **https://app.knovel.com/hotlink/itble/rcid:kpKS000009/id:kt00395F16/knovel-sampler/basic-physical-properties**, (Accessed 15th July 2024).
64 A. Ujčić, M. Sobótka, M. Šlouf, A. Różański and K. Szustakiewicz, *Polym. Test.*, 2023, **118**, 107906.
65 P. K. Parhi, *J. Chem.*, 2013, **2013**, 618236.
66 T. K. Dash and V. B. Konkimalla, *J. Controlled Release*, 2012, **158**, 15–33.
67 Q. L. Loh and C. Choong, *Tissue Eng., Part B*, 2013, **19**, 485–502.
68 K. S. McGuire, A. Laxminarayan and D. R. Lloyd, *Polymer*, 1995, **36**, 4951–4960.
69 S. Manholi and S. Athiyanathil, *J. Appl. Polym. Sci.*, 2022, **139**, 51720.
70 G. Van Eygen, S. Keuppens, X. De Breuck, B. Swankaert, P. Boura, E. Loccufier, J. Kosek, D. Ramasamy, F. Nahra, A. Buekenhoudt, K. De Clerck, B. Van der Bruggen and P. Luis, *Sep. Purif. Technol.*, 2025, **352**, 128192.